Mean-field theory of active electrolytes: Dynamic adsorption and overscreening

Derek Frydel

Department of Chemistry, Federico Santa Maria Technical University, Campus San Joaquín, Santiago, Chile

Rudolf Podgornik

School of Physical Sciences and Kavli Institute for Theoretical Sciences, University of Chinese Academy of Sciences, Beijing 100049, China;
CAS Key Laboratory of Soft Matter Physics, Institute of Physics, Chinese Academy of Sciences, Beijing 100190, China;
Department of Physics, Faculty of Mathematics and Physics, University of Ljubljana, 1000 Ljubljana, Slovenia;
and Department of Theoretical Physics, J. Stefan Institute, 1000 Ljubljana, Slovenia

We investigate active electrolytes within the mean-field level of description. The focus is on how the double-layer structure of passive, thermalized charges is affected by active dynamics of constituting ions. One feature of active dynamics is that particles adhere to hard surfaces, regardless of chemical properties of a surface and specifically in complete absence of any chemisorption or physisorption. To carry out the mean-field analysis of the system that is out of equilibrium, we develop the "mean-field simulation" technique, where the simulated system consists of charged parallel sheets moving on a line and obeying active dynamics, with the interaction strength rescaled by the number of sheets. The mean-field limit becomes exact in the limit of an infinite number of movable sheets.

I. INTRODUCTION

The mean-field approximation is the most common tool in dealing with electrostatic systems in the weak-coupling regime [1–3]. The suitability of the mean-field collective description to electrostatics stems from the long-range nature of Coulomb interactions; because each particle interacts with all other particles in a system; this, in turn, brings about significant suppression of fluctuations in systems under standard conditions [4,5].

In recent years, the mean-field analysis has been extended to ions with inner structure to include an ever larger class of emerging systems. These extensions incorporate steric effects [6–9], multipolar interactions [10,11], polarizability [12,13], penetrability [14–20], nonspherical shapes such as that of dumbbell ions [21–24], and the various combinations of the above extensions [25].

In the present work we extend the mean-field approximation not to different ionic structures, but to different dynamics. Thus, point ions instead of being Brownian are now active particles, with trajectories characterized by constant velocity and diffusing orientation, giving rise to orientational persistence. A peculiar feature of active dynamics, and the direct consequence of orientational persistence combined with overdamped dynamics, is that particles adhere to hard surfaces [26] (see Fig. 1). Such "dynamic adsorption" is different from chemisorption and physisorption, which depend on the chemistry of a surface [27–36].

The signature of "dynamic adsorption" is the emergence of a divergent density profile at the location of a hard surface. From the mathematical point of view, the divergence ensures the continuity of a density, at the point where the density profile of free particles merges with the Dirac delta function representing the distribution of adsorbed particles. Physically, the divergence arises due to newly released particles, which tend to have orientations nearly parallel to a wall. Such particles have a tendency to "linger" in the vicinity of a wall, giving rise to an observed divergence.

In case of ions, "dynamic adsorption" will naturally modify the surface charge of a wall. It is the aim of this paper to investigate this phenomenon as well as other dynamic contributions to the structure and properties of a double layer, within the mean-field level of description.

Part of the challenge in achieving these goals is technical. The stationary distributions of active particles cannot be obtained from their corresponding Boltzmann weights. In consequence, even the simple case of noninteracting active particles is not amenable to analytical solutions based on the Fokker-Planck equation [37–39], and the dynamic simulations still offer the most direct way to analyze these systems.

In the present work we develop the "mean-field simulation," which allows us to study charged systems with plane geometry within the mean-field level of description. The simulated system consists of charged sheets moving on a line; thus, it is strictly one-dimensional. The mean-field limit corresponds to infinitely many sheets with an infinitesimal surface charge, while the total charge density remains fixed. The method is designed specifically for planar geometry. The "mean-field simulation" developed in this work is, therefore, not directly transferable to other geometries.

The present work is organized as follows. In Sec. II we review general properties of active particles. In Sec. III we go over some of the results for active particles in a gravitational field. In Secs. IV and V we develop the mean-field simulation for active ions. In Secs. VI and VII we proceed to apply that method to study various systems and their variations. Finally, in Sec. VIII we conclude the work.
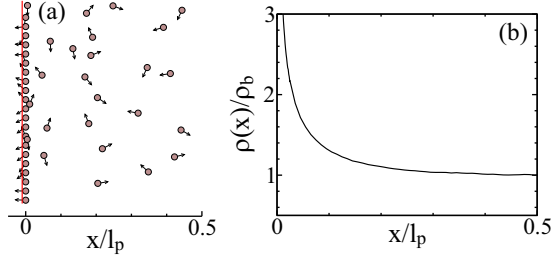
FIG. 1. (a) A snapshot of active ideal particles in two dimensions near a confining hard wall at $x = 0$, and (b) the corresponding stationary distribution normalized by a bulk density ρ_b. In overdamped dynamics particles are not reflected in contact with a wall; instead they remain trapped until an orientational vector diffuses to the direction away from a wall. Released particles have initially almost parallel orientation with a wall. This causes a released particle to "linger" in the vicinity of a wall, giving rise to a divergent density profile.

II. PRELIMINARIES

The motion of an active-Brownian particle is characterized by a constant velocity v_0 and a diffusion of an orientational vector $\mathbf{n}(\theta, \phi) = (\sin \theta \cos \phi, \sin \theta \sin \phi, \cos \theta)$ over a spherical surface of unit radius with a rotational diffusion constant D_r (units of 1/time). Diffusion of an orientation vector leads to directional persistence, resulting in the exponentially decaying orientation-orientation correlation function $\langle \mathbf{n}(0) \cdot \mathbf{n}(t) \rangle = e^{-t/\tau_p}$, where

$$\tau_p = \frac{1}{d-1} \frac{1}{D_r} \tag{1}$$

is the persistence time and d is a system dimensionality [40]. This leads to a translational persistence with the persistence length given by

$$l_p = v_0 \tau_p. \tag{2}$$

If a distance that an active particle covers in time t is $\mathbf{r}(t) = v_0 \int_0^t ds \, \mathbf{n}(s)$, then the expression for the mean-squared displacement evaluates as

$$\langle r^2(t) \rangle = 2l_p^2 \left[\frac{t}{\tau_p} + e^{-t/\tau_p} - 1 \right]. \tag{3}$$

The above expressions span two limits. At short times the motion is ballistic, $\langle r^2(t) \rangle \approx l_p^2 (t/\tau_p)^2$. Then at long times it is diffusive,

$$\langle r^2(t) \rangle \approx \left(\frac{l_p^2}{\tau_p} \right) t, \tag{4}$$

with the "effective" translational diffusion constant given by

$$D_{\text{eff}} = \frac{1}{d} \frac{l_p^2}{\tau_p}. \tag{5}$$

Using the Einstein relation $D = k_B T / \zeta$, where ζ designates the friction coefficient of a medium, it becomes possible to define an "effective" temperature:

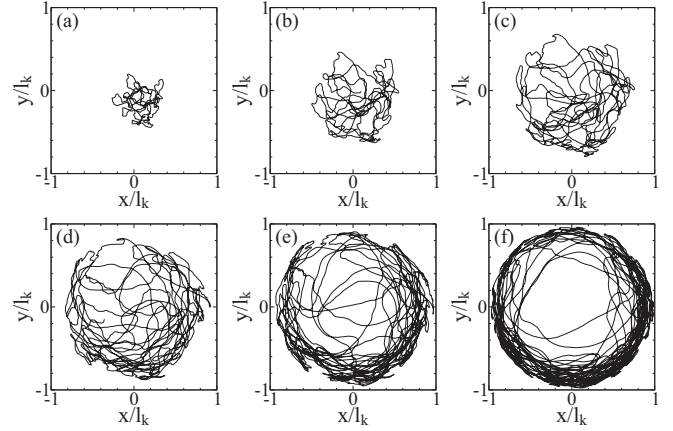$$k_B T_{\text{eff}} = \frac{1}{d} \frac{\zeta l_p^2}{\tau_p}. \tag{6}$$

FIG. 2. Trajectories for a single active particle in a harmonic trap for different ratios l_p / l_k (0.1, 0.25, 0.5, 1, 2, 4). The simulation is carried out in two dimensions to facilitate visualization. The duration of each trajectory is $100\tau_p$.

The above temperature expression will be used in subsequent sections for comparing the results for active particles with those for passive particles.

The temperature expression in Eq. (6) is not to be confused with the equilibrium temperature of a medium in which active particles are immersed. The medium contributes two effects. First, it is perfectly dissipative, leading to overdamped (non-Newtonian) dynamics. Second, it contributes thermal fluctuations. In the present study, the temperature of a medium is set to zero, in order to isolate the contributions due to active dynamics.

To emphasize the essential role of overdamped dynamics in the phenomena of dynamic adsorption, we consider a particle propagating through a scattering medium, that is, a medium of randomly distributed, small-angle, elastic point scatterers [37]. The velocity of a scattered particle is constant while its direction fluctuates. Up to this point, this is precisely what occurs for active particles. The scattering medium, however, is not dissipative, and dynamically the system is Newtonian. The two systems start to deviate in presence of external potentials or interparticle interactions. In consequence, the scattering system does not produce dynamic adsorption.

A. Harmonic confinement

To demonstrates the significance of the persistence length, we consider a single active particle inside a harmonic trap [41]. We define the size of a trap, l_k, as a distance measured from the trap center, beyond which an active particle cannot penetrate. This distance corresponds to the balance between the two forces: the particle intrinsic force, ζv_0, and the trap's restoring force, $F = -kr$. The condition of balance yields $l_k = \zeta v_0 / k$.

Figure 2 shows a number of trajectories of an active particle inside a trap for different ratios l_p / l_k. The figures are plotted in units of l_k. As confinement increases, the trajectories become increasingly restricted to the border region of a trap at $r/l_k = 1$. Figure 3 shows the corresponding stationary distributions.

For the lowest ratio l_p / l_k, the distribution is nearly Gaussian, $\sim e^{-kr^2/(2k_B T)}$, with $k_B T$ given in Eq. (6). As the ratio l_p / l_k
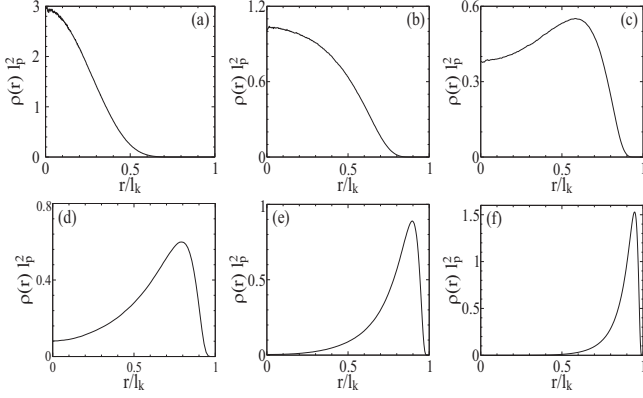
FIG. 3. Stationary distributions corresponding to Fig. 2.

decreases, the distribution shifts toward the edge of a wall. For $l_p/l_k = 4$, an active particle is almost entirely confined to the edge of a trap.

The situation is analogous to the packing problem of a wormlike chain inside a circular hard-wall confinement [42,43]; see Fig. 4. As the persistence length of a wormlike chain increases, a polymer becomes less elastic, and the energetically least costly configuration corresponds to packing along the inner circumference of a trap.

A similar breakdown of Boltzmann statistics is expected to occur in any system with some confinement length, at the point where the confinement length becomes comparable with the persistence length.

B. Dynamic simulation

1. Dynamic integration

Dynamic simulations use the time integration, for $z(t)$ and $\theta(t)$, updated at discrete times. The present work uses the Euler integrator, which is the simplest update algorithm:

$$z(t + \Delta t) = z(t) + \left\{ v_0 \cos \theta(t) + \frac{F[z(t)]}{\zeta} \right\} \Delta t, \quad (7)$$

$$\theta(t + \Delta t) = \theta(t) + \hat{\xi}(t)\sqrt{2D_r \Delta t} + D_r \cot \theta(t)\Delta t. \quad (8)$$

$F(z)$ in the first equation denotes an external force. Then the term $\hat{\xi}(t)$ in the second equation represents a random value generated at each step and taken from a Gaussian distribution with zero and unity variance. The second equation contains a deterministic term $D_r \cot \theta$, even if there is no such
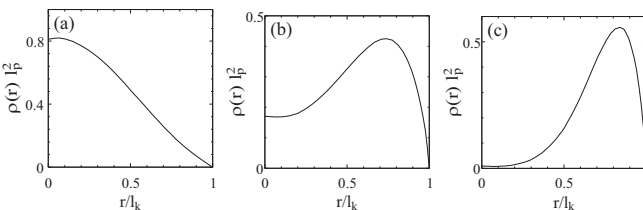

FIG. 4. Distribution of a wormlike chain inside a circular hard-wall trap with radius $R = l_k$. Figures are from Ref. [42] for $l_p/l_k = 2,4,8$. As $l_p/l_k \to 0$ (the weak confinement limit) the distributions approach those of a Gaussian chain model.

deterministic torque [44–46]. This term is not present in $d = 2$, and it arises in $d = 3$ to account for a spherical surface over which a vector **n** diffuses. The integration over $x(t)$, $y(t)$, and $\phi(t)$ is not required for a planar geometry.

Straightforward integration in Eq. (8) can be problematic for orientations near the two poles, $\theta = 0$ and $\theta = \pi$, where the deterministic term diverges. This problem is corrected by integrating instead an orientation vector in Cartesian coordinates. Since for the wall geometry only n_z is relevant, the Euler integrator for this component of an orientation is [46]

$$n_z(t + \Delta t) = n_z(t) - \hat{\xi}_1(t)\sin\theta(t)\sqrt{2D_r\Delta t} \\ - D_r[\hat{\xi}_1^2(t) + \hat{\xi}_2^2(t)]n_z(t)\Delta t, \quad (9)$$

where $n_z = \cos\theta$. Note that now there are two random numbers, $\hat{\xi}_1(t)$ and $\hat{\xi}_2(t)$, generated at each step.

2. Boundary conditions

Dynamic simulations are carried out within an interval $z \in (0,L)$. Each time a particle crosses a boundary at $z = 0$ or $z = L$, it is moved to the location of a boundary in the same step. A possibility of a particle being bounced from a wall is prevented by overdamped dynamics.

Because a particle can move away from a wall only if its orientation points in the direction away from a wall, and because such reorientation does not occur instantaneously due to orientational relaxation, a particle that arrives at a wall is considered as adsorbed, at least for the time being. This procedure is repeated until a velocity vector points away from a wall.

The interval length of a simulation box, L, varies from system to system. For a gravitational system considered in the next section $L \to \infty$, as particles are naturally confined by a gravitational force.

3. Reduced units

As the unit of length and time we take l_p and τ_p. Consequently, the reduced position on the z axis is $z^* = z/l_p$, the reduced time is $t^* = t/\tau_p$, and a reduced density is $\rho^* = l_p^3\rho$. Furthermore, the unit of force is ζv_0 and the reduced force is $F^* = F/(\zeta v_0)$ and the reduced pressure is $P^* = Pl_p^2/(\zeta v_0)$. The time step that we use is $\Delta t^* = 0.001$.

III. GRAVITATIONAL FORCE

Prior to considering charged particles, we review results for noninteracting active particles in the gravitational field, $F = -G$. The Euler integrators for the position and orientation vector are

$$z^*(t^* + \Delta t^*) = z^*(t^*) + [n_z(t^*) - \gamma_G]\Delta t^*, \quad (10)$$

where the reduced gravitational force is

$$\gamma_G = \frac{G}{\zeta v_0}, \quad (11)$$

and

$$n_z(t^* + \Delta t^*) = n_z(t) - \hat{\xi}_1(t)\sin\theta(t^*)\sqrt{\Delta t^*} \\ - \tfrac{1}{2}[\hat{\xi}_1^2(t^*) + \hat{\xi}_2^2(t^*)]n_z(t^*)\Delta t^*, \quad (12)$$
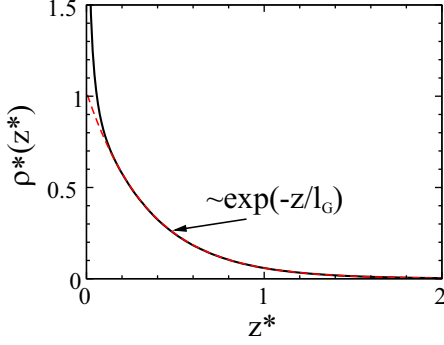
where both equations are expressed in reduced units.

FIG. 5. The stationary distribution of active-Brownian particles in the gravitational field with strength $\gamma_G = 0.5$. The system is confined by a wall at $z^* = 0$. The profile is obtained from a dynamic simulation, and the fit at a far field demonstrates exponential decay.

Ideal active particles in gravitational field in two dimensions have been considered in Refs. [38,39]. The analysis was based on separation of variables, leading to a Mathieu differential equation for the orientational counterpart [47–49]. A dominant exponential decay could be obtained from the lowest eigenfunction. For active particles in gravitational field in three-dimensional space, separation of variables does not generate the Mathieu equation, and it is not clear if analytical results in terms of known functions are available. Here we don't attempt analytical analysis and limit ourselves to a simple presentation of simulation results.

Figure 5 shows an average stationary distribution for the gravitational strength $\gamma_G = 0.5$. The profile exhibits two distinct regions, the near-field divergence (implying dynamic adsorption) followed by an exponential decay. Due to adsorption, the integrated density of free particles is less than the total number of particles in a system, $\int_0^\infty dz^* \, \rho^*(z^*) < n$.

In Fig. 6 we plot the quantity $g = 1 - n_A/n$, where g corresponds to a fraction of free particles, as a function of γ_G. For no adsorbed particles $g = 1$, and for all adsorbed particles $g = 0$. The monotonically decreasing behavior of g is expected, but the surprising feature of the plot is that g vanishes beyond $\gamma_G = 1$. For $\gamma_G = 1$ and beyond, all the particles are adsorbed. The adsorption is complete and permanent. This has a straightforward explanation. For $\gamma_G > 1$, particle velocities
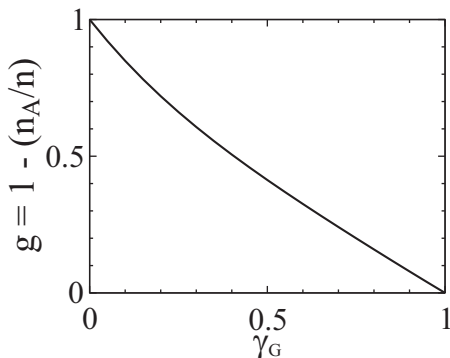

FIG. 6. The fraction of free (nonadsorbed) particles as a function of γ_G.

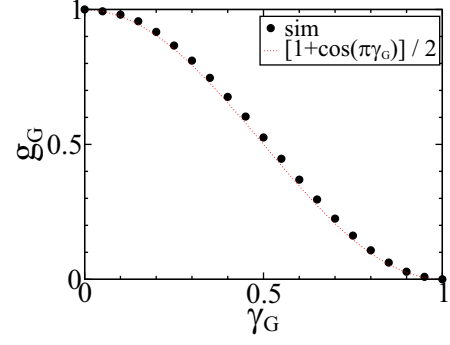

FIG. 7. The renormalization constant g_G, introduced in Eq. (14), as a function of γ_G. The data points are compared to the empirical functional form $(1 + \cos \gamma_G \pi)/2$.

in the z direction can only be negative, regardless of their orientations. But because particles cannot go beyond $z = 0$, they become permanently trapped. Their motion occurs only in the plane of a wall.

Next we consider the far-field behavior of a distribution. The fact that it is exponential is not surprising, that is, $\rho(z) \sim e^{-z/l_G}$. A more interesting fact to look into is the scaling of l_G as a function of γ_G. It is reasonable to assume that in the limit $\gamma_G \to 0$ one recovers the Boltzmann-like behavior, where $\rho(z) \sim e^{-Gz/k_B T}$, because l_G and therefore the confinement is large, $l_G \to \infty$. Substituting for $k_B T$ in Eq. (6) we get $\rho^*(z^*) \sim e^{-3\gamma_G z^*}$, so that the decay length is

$$\lim_{\gamma_G \to 0} \frac{l_G}{l_p} = \frac{1}{3\gamma_G}. \qquad (13)$$

This scaling is confirmed by simulations for small γ_G. But as γ_G increases, and the confinement decreases, l_G start to deviates from the behavior in Eq. (13). To capture the deviations from the Boltzmann behavior, we introduce the dimensionless parameter g_G, referred to as the renormalization constant, and rewrite the expression in Eq. (13) as

$$\frac{l_G}{l_p} = \frac{g_G}{3\gamma_G}. \qquad (14)$$

In Fig. 7 we plot g_G as a function of γ_G. The observation is that g_G decreases with the strength of a gravitational force. The explanation is that as γ_G increases, the orientations that generate positive velocity (velocity away from a wall) become reduced. The behavior of g_G is roughly trigonometric, $(1 + \cos \gamma_G \pi)/2$. Beyond $\gamma_G = 1$, g_G vanishes.

As the final point, we investigate the link between adsorbed particles and pressure [50–53]. In the case of active particles, pressure is calculated by counting the number of adsorbed particles and then taking into account their orientations. The reason is that only adsorbed particles exert force on a wall. The force is proportional to a particle velocity in the direction toward a wall. In reduced units, this is expressed as

$$\frac{l_p^2 P}{\zeta v_0} = 2\pi n_A \int_0^\pi d\theta \, \sin\theta (\gamma_G - \cos\theta) \, \rho_A(\theta), \qquad (15)$$

where $\rho_A(\theta)$ is the angular distribution of adsorbed particles, normalized as $2\pi \int_0^\pi d\theta \, \sin\theta \rho_A(\theta) = 1$. One could evaluate the integral by considering the Fokker-Planck equation of the

present system; see Appendix A for details. However, knowing that a force exerted by active particles must be equal and opposite to the gravitational force exerted on the same particles, we guess the following result:

$$\frac{l_p^2 P}{\zeta v_0} = \gamma_G n, \tag{16}$$

which is confirmed by simulations.

IV. THE MEAN-FIELD TREATMENT OF ACTIVE IONS

In the case of active ions, there is no gravitational field, but a similar constant force arises from a uniform surface charge, σ_c, interacting with ions on account of their charge $\pm q$. In addition to the one-body constant force, there are now many-body interactions due to Coulomb forces between ions.

Within the mean-field approximation, an ion, instead of interacting with individual ions, interacts with an average charge distribution due to all ions. This reduces a many-body to a one-body problem. Given a two-component symmetric electrolyte $q{:}q$, the averaged one-body force is

$$F_\pm(z) = \mp q \frac{d\psi(z)}{dz}, \tag{17}$$

where $\psi(z)$ is the average electrostatic potential. Using the Poisson relation,

$$\epsilon \frac{d^2\psi(z)}{dz^2} = -\rho_c(z), \tag{18}$$

where $\rho_c(z) = q\rho_+(z) - q\rho_-(z)$, $\rho_\pm(z) = \int_0^\pi d\theta\, \rho_\pm(z,\theta)$, and ϵ is the dielectric constant of a medium, the force can be expressed in terms of a charge density distribution as

$$F_\pm(z) = \mp \frac{q}{\epsilon} \int_z^\infty dz'\, \rho_c(z'), \tag{19}$$

where the neutrality constraint requires

$$\int_0^\infty dz\, \rho_c(z) = -\sigma_c. \tag{20}$$

V. THE MEAN-FIELD SIMULATION

For the case of passive ions, the mean-field framework is completed by expressing the charge density using the Boltzmann weight, $\rho_c \approx q c_s (e^{-\beta q\psi} - e^{\beta q\psi})$, leading to the Poisson-Boltzmann equation. For active ions there is no equivalent of the Boltzmann factor, and there is no available expression for ρ_c in terms of ψ.

To overcome this problem, we work with instantaneous distributions,

$$\hat{\rho}_+(z) = \left(\frac{\sigma_c}{qn}\right) \sum_{i=1}^{n_s} \delta(z_i^+ - z), \tag{21}$$

$$\hat{\rho}_-(z) = \left(\frac{\sigma_c}{qn}\right) \sum_{i=1}^{n+n_s} \delta(z_i^- - z), \tag{22}$$

where the weight factor $\sigma_c/(qn)$ determines the contribution of each particle to a density and ensures correct units. Note that there are more counterions than coions, $n_- = n_s + n$ and $n_+ = n_s$, where n_s is the number of salt ions and n is the

excess of counterions needed to neutralize the surface charge $\sigma_c \geqslant 0$. The mean-field distributions correspond to averaged instantaneous distributions:

$$\rho_\pm^{\mathrm{mf}}(z) = \langle \hat{\rho}_\pm(z) \rangle. \tag{23}$$

Using the above expressions, the instantaneous charge density, defined as $\hat{\rho}_c(z) = q\hat{\rho}_+(z) - q\hat{\rho}_-(z)$, is written as

$$\hat{\rho}_c(z) = q\left(\frac{\sigma_c}{qn}\right) \left[\sum_{i=1}^{n_s} \delta(z_i^+ - z) - \sum_{i=1}^{n_s+n} \delta(z_i^- - z) \right], \tag{24}$$

where the charge of each particle is rescaled by n and the total charge density correctly integrates as

$$\int_0^\infty dz\, \hat{\rho}_c(z) = -\sigma_c, \tag{25}$$

satisfying the neutrality constraint.

Now it becomes possible to write the expression of force, analogous to that in Eq. (19),

$$F(z_i^\pm) = \mp \frac{q}{\epsilon} \frac{\sigma_c}{n} A(z_i^\pm), \tag{26}$$

where

$$A(z_i^\pm) = \sum_{j=1}^{n_s} H(z_i^\pm - z_j^+) - \sum_{j=1}^{n_s+n} H(z_i^\pm - z_j^-), \tag{27}$$

and

$$H(z) = \begin{cases} 1, & \text{if } z > 0 \\ \frac{1}{2}, & \text{if } z = 0 \\ 0, & \text{if } z < 0 \end{cases} \tag{28}$$

is the step function. The term $\sum_j H(z_i - z_j)$ counts the number of particles within the interval $z_i \leqslant z < \infty$. Because $H(0) = 1/2$, a particle that defines the lower limit of the interval contributes one half to the total count.

Once the forces in Eqs. (26) and (27) are evaluated, one uses the Euler integrator

$$z_i^\pm(t + \Delta t) = z_i^\pm(t) + \left\{ v_0 \cos\theta_i(t) - \frac{F[z_i^\pm(t)]}{\zeta} \right\} \Delta t, \tag{29}$$

plus the expressions for n_z in Eq. (9).

The equations written above actually describe a system of charged parallel sheets moving along the z axis and obeying active dynamics in that direction. The surface charge of each plate is $\pm q/A$, where $A = qn/\sigma_c$ is the surface area, and the magnitude of the interaction force between any two sheets is $f_{12} = q^2/(2\epsilon A) = q\sigma_c/(2\epsilon n)$. The strength of the interactions, therefore, depends on the number of particles n. (In addition, there is a fixed plate at $z = 0$ with the surface charge σ_c.) The mean-field solution corresponds to the limit $n \to \infty$, where interactions between individual sheets, f_{12}, vanish. If this limit is not satisfied, the distributions of the simulated model should no longer correspond to the mean-field approximation. To ensure that the procedure and the simulation technique is accurate, in Appendix B we apply it to the case of passive ions, for which analytical expressions are available, so that accuracy can be easily checked. The results indicate that already $n = 100$ particles yield accurate mean-field distributions.

The mean-field simulations have previously been used in a number of systems. For example, to study the Hamiltonian plasma model comprised of Coulomb sheets in a fixed neutralizing background [54]. In several versions of the model, the sheets can either pass through one another or undergo elastic collisions. A similar technique has been applied to study the XY-Heisenberg model in periodic boundary conditions [55]. The method is referred to as the Hamiltonian mean-field model due to the underlying Hamiltonian dynamics. The Hamiltonian treatment of our system, that is, the switch from active-overdamped to passive-Newtonian dynamics, would lead to an altogether different physical interpretation, with the latter case representing a plasma system. Such a model should give rise to a system that does not relax to a Boltzmann distribution, but for different physical reasons connected with the long-range interactions and the absence of a thermodynamic limit [56].

A. Calculation of forces and the use of a position index

Computationally, the most demanding step in the algorithm is the calculation of forces acting on every particle at each time step. To reduce its computational effort, we implement the following procedure. Each particle is assigned two indices, l and k. The first index is simply a label. The numbers $1 \leqslant l \leqslant n_s + n$ are reserved for counterions and $n_s + n < l \leqslant n_T$ for coions. The other index determines the location of a particle within a sequence:

$$0 \leqslant z_{n_T} < z_{n_T-1} < \cdots < z_k < \cdots < z_2 < z_1 < \infty. \quad (30)$$

This index is not permanent but is updated at each time step. As only a handful of particles exchange their relative positions in the sequence, the update is quick and scales as $O(n_T)$. The procedure consists of a loop that compares the positions z_k and z_{k+1} for every k. If $z_k \geqslant z_{k+1}$ is false, the two indices are exchanged. The loop is repeated until the condition $z_k \geqslant z_{k+1}$ is true for every k. Once the sequence is established, it is trivial to calculate forces. The computation effort of the algorithm scales as $O(n_T)$.

B. Reduced units

In the rest of the paper we use the reduced units. The dimensionless strength of electrostatic interactions is

$$\gamma_q = \frac{1}{\zeta v_0} \left(\frac{q \sigma_c}{\epsilon} \right), \quad (31)$$

and the reduced force is $F^* = F/(\zeta v_0)$. Densities are expressed in units $\sigma_c/(q l_p)$, so that the reduced density is

$$\rho_{\pm}^* = \rho_{\pm} \left(\frac{q l_p}{\sigma_c} \right), \quad (32)$$

and the dimensionless salt strength is

$$\gamma_{c_s} = c_s \left(\frac{q l_p}{\sigma_c} \right), \quad (33)$$

where c_s is the salt concentration in a bulk. One can also define a reduced charge density:

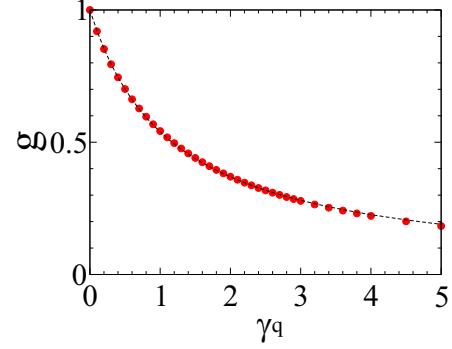$$\rho_c^* = \rho_c \left(\frac{l_p}{\sigma_c} \right). \quad (34)$$

FIG. 8. The renormalization constant, $g = 1 - n_A/n$, as a function of γ_q. The data points obtained from the mean-field simulation are fitted to a functional form $g = (1 + \gamma_q/\gamma_{\text{sat}})^{-1}$, where $\gamma_{\text{sat}} \approx 1.17$.

The units of length and time, as before, are the persistence length and time, l_p and τ_p, respectively. Finally, the Euler integrators become

$$z_i^{*\pm}(t + \Delta t) = z_i^{*\pm}(t) + \{n_{z_i}(t^*) - \gamma_q A[z_i^{\pm}(t)]\} \Delta t^*, \quad (35)$$

with $A(z_i^{\pm})$ defined in Eq. (27). Then n_{z_i} is updated according to Eq. (9).

VI. ACTIVE COUNTERIONS

For the counterion-only case the concentration of salt is set to zero, that is, $n_s = 0$, then $n_- = n$ and $n_+ = 0$. Due to dynamic adsorption of counterions on a charged wall, a surface charge of a wall becomes reduced, with the effective surface charge given as $\sigma_{\text{eff}} = g \sigma_c$, where $g = 1 - n_A/n$ is the renormalization constant. Due to this renormalization, the force exerted on adsorbed particles needs to be renormalized at each time step, $F(0) = -\hat{g} \gamma_q$, where $\hat{g}$ is the instantaneous renormalization, such that $g = \langle \hat{g} \rangle$. Without adsorption, $F(0) = -\gamma_q$.

In Fig. 8 we plot g as a function of γ_q. The plot indicates that the effective surface charge decreases with the strength of electrostatic interactions, and a simple fit to the data points reveals the decay rate of g to be algebraic, as $\sim \gamma_q^{-1}$. Consequently, the effective surface charge σ_{eff} must saturate in the limit $\sigma_c \to \infty$ [see the definition for γ_q in Eq. (31)].

Before analyzing the distribution of active counterions, we review the mean-field results for passive ions. The mean-field charge distribution of passive counterions is

$$\rho_c(z) = \frac{\sigma_c/\lambda_{GC}}{(1 + z/\lambda_{GC})^2}, \quad (36)$$

where

$$\lambda_{GC} = \frac{2\epsilon k_B T}{e^2 \sigma_c} \quad (37)$$

is the Gouy-Chapman length. Using Eq. (6) to substitute for $k_B T$, the Gouy-Chapman length for active particles is

$$\frac{\lambda_{GC}}{l_p} = \frac{2}{3} \frac{1}{\gamma_q}. \quad (38)$$

In the limit $\gamma_q \to 0$ the distributions for passive and active particles converge, apart for the divergence at $z = 0$, which is
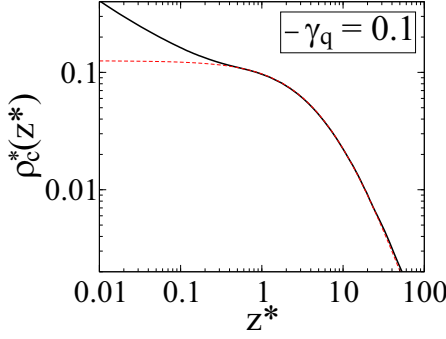
FIG. 9. Density distribution of counterions for $\gamma_q = 0.1$. The profile obtained from a simulation is compared to a fit in Eq. (39) with $g_{\text{fit}} \approx 0.91$, determined by matching of the far-field regions.

absent for passive ions. In Fig. 9 we plot $\rho_c(z)$, obtained from a simulation for $\gamma_q = 0.1$, and compare it with the ansatz

$$\rho_c(z) = \frac{g_{\text{fit}}^2 \sigma_c / \lambda_{GC}}{(1 + g_{\text{fit}} z / \lambda_{GC})^2}, \tag{39}$$

where the fitting parameter for $\gamma_q = 0.1$ is $g_{\text{fit}} \approx 0.91$. A small renormalization is the result of ion adsorption.

The ansatz in Eq. (39) becomes less accurate for larger γ_q. A more accurate fit is $\rho_c^*(z) = \frac{a}{b + cz^* + z^{*2}}$; see Fig. 10. The ansatz does not modify the asymptotic behavior, which is still $\sim z^{-2}$, but it is significantly more accurate in the intermediate region.

Equation (38), obtained from the mean-field for passive ions, suggests $a = 2/(3\gamma_q)$. We find this relation to be correct not only in the limit $\gamma_q \to 0$, but for any arbitrary value of γ_q. This then means that the asymptotic region is not modified by counterion adsorption, and far away from a wall the distinction between active versus passive dynamics becomes irrelevant— at least for a counterion-only system.

VII. ACTIVE ELECTROLYTE

Next we consider a charged wall in contact with electrolyte. The concentration of salt c_s, in the mean-field simulation, is controlled through n_s. Dissociation of salt brings into the system additional counterions but also coions. Because a system is filled with salt ions, one must account for the
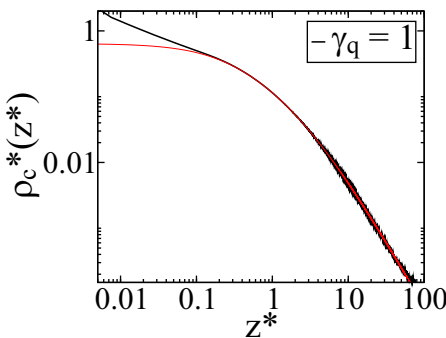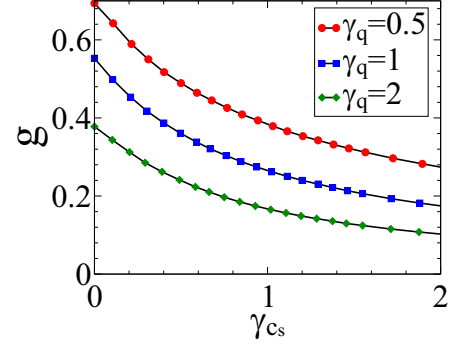

FIG. 11. The renormalization constant, $g = 1 - (n_A^- - n_A^+)/n$, as a function of γ_{c_s} for different values of γ_q. The results are from the mean-field simulation.

osmotic pressure and its contribution to dynamic adsorption of counterions as well as the concurrent adsorption of coions.

The renormalization factor now is defined as $g = 1 - (n_A^- - n_A^+)/n$, where n_A^- and n_A^+ is the number of adsorbed counterions and coions, respectively. Figure 11 shows simulation data points for g as a function of γ_{c_s} for a number of different γ_{c_s}. The results indicate increased adsorption of charge with increased concentration of salt: the larger the concentration of salt, the larger the osmotic pressure pushing particles toward a wall. Yet the suppression of charge is slow due to the concurrent adsorption of coions, which reverse the effect of adsorbed counterions.

In Fig. 12 we plot separate contributions of g, that is, n_A^- and n_A^+, as a function of γ_{c_s}. There are a number of interesting observations. First, the number of adsorbed counterions exceeds that of a surface charge, that is, $n_A^-/n > 1$, at roughly $\gamma_{c_s} > 1$, which by itself should imply charge inversion. However, charge inversion is prevented by the concurrent adsorption of coions.

If we look at the adsorption rates, that is, $r^- = \frac{d}{d\gamma_{c_s}}(\frac{n_A^-}{n})$ and $r^+ = \frac{d}{d\gamma_{c_s}}(\frac{n_A^+}{n})$, we find that r^- approaches r (which is the rate of adsorption for neutral particles determined to be $r \approx 0.55$) from above, while r^+ approaches r from below. In the limit $\gamma_{c_s} \to \infty$ the two rates converge, $r^- = r^+ = r$, implying that adsorption is entirely determined by osmotic pressure.

Next we look into the far-field region of charge distributions. For passive ions, the Debye screening parameter κ of the
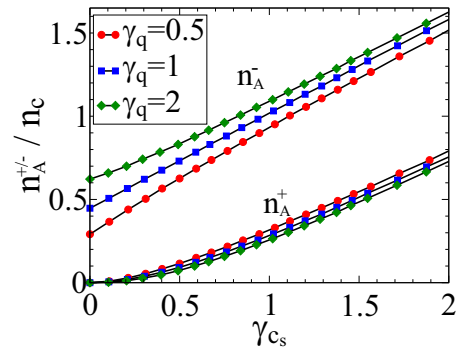

FIG. 10. Density distribution of counterions for $\gamma_q = 1$ together with a fit $\rho_c^*(z) = \frac{a}{1 + bz^* + cz^{*2}}$.

FIG. 12. The adsorption of counterions, n_A^-, and coions, n_A^+, as a function of γ_{c_s} for different γ_q.
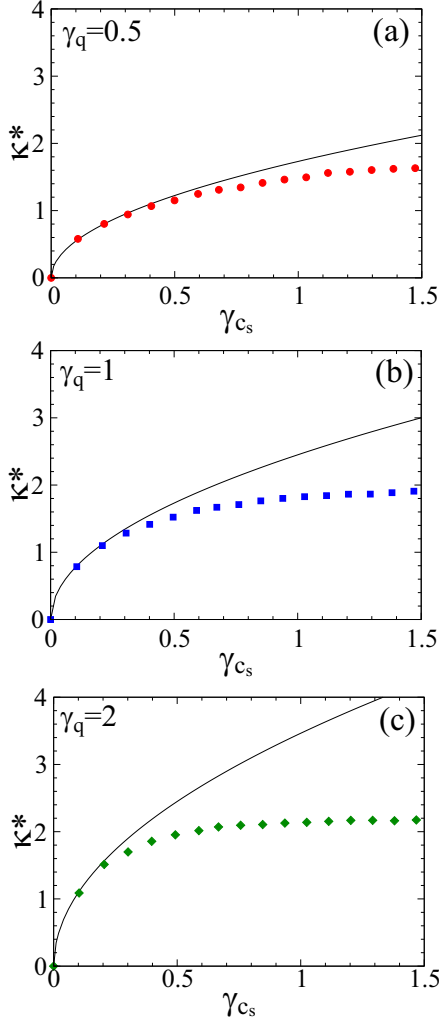
FIG. 13. The screening parameter κ for active ions. The data points from simulations are plotted against the analytical expression in Eq. (41).

exponential decay (related to a screening length as $\lambda_D = \kappa^{-1}$) is

$$\kappa = \sqrt{\frac{2c_s q^2}{\epsilon k_B T}}. \tag{40}$$

Using Eq. (6) to substitute for $k_B T$, we get

$$l_p \kappa = \sqrt{6\gamma_q \gamma_{c_s}}. \tag{41}$$

For the counterion-only case, the far-field algebraic decay agreed with that for passive ions, so that the profiles for passive and active ions differ only in the near-field and intermediate regions. Whether Eq. (41) accurately describes the far-field decay for electrolytes, we examine next.

In Fig. 13 we plot κ obtained by fitting charge distributions to the functional form $\rho(z) \sim e^{-\kappa z}$, and then compare the plots with the expression in Eq. (41). For low concentrations of salt, $\gamma_{c_s} \to 0$, the results for active particles agree with Eq. (41). But as γ_{c_s} increases, the two plots begin to deviate, where active ions show reduced screening, which implies a more diffuse
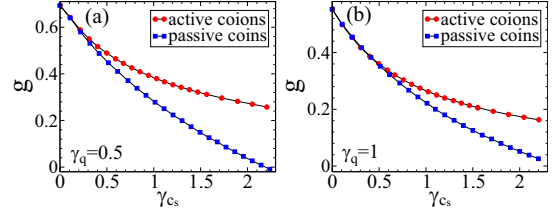
double layer. The screening parameter, furthermore, appears to saturate at a value slightly above $\kappa^* = 2$.

A plausible explanation of a more diffuse double layer in an active system is some sort of competition between the screening and the persistence length. A persistence length sets a limit on how compressed a double layer may become.

As the last point, we provide the mean-field expression of pressure for electrolytes,

$$\left(\frac{q}{\zeta v_0 \sigma_c}\right) P = \frac{1}{2}\gamma_q + \frac{2}{3}\gamma_{c_s}, \tag{42}$$

where the first term accounts for electrostatic contributions and the second term accounts for an (ideal-gas) osmotic pressure.

A. Passive coions

In the above example all ions are active. In this section we consider a mixture of passive coions and active counerions. As passive coions do not get adsorbed, they don't contribute to the renormalization of a surface charge. We set the diffusion constant of passive coions to be the same as that of active counterions, $D = D_{\text{eff}}$, with D_{eff} defined in Eq. (5).

In Fig. 14 we plot the renormalization constant, $g = 1 - n_A^-/n$, for the above described system.

In comparison to the results in Fig. 11, the renormalization constant becomes zero at $\gamma_{c_s} \approx 2.2$ (for $\gamma_q = 0.5$) and $\gamma_{c_s} \approx 2.4$ (for $\gamma_q = 1$), then beyond, g changes sign, indicating a "surface charge inversion" as adsorbed counterions overcompensate a bare surface charge.

In Fig. 15 we plot charge densities for different values of γ_{c_s} (for $\gamma_q = 0.5$). At $\gamma_{c_s} = 1.3$ the charge distribution changes sign, even before the "surface charge inversion" at $\gamma_{c_s} \approx 2.2$. We refer to this as "overscreening" to distinguish it from

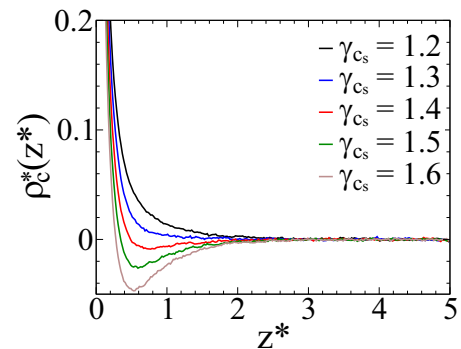FIG. 14. Renormalization constant g as a function of γ_{c_s} for $\gamma_q = 0.5$ and $\gamma_q = 1$.

FIG. 15. The charge density profiles for $\gamma_q = 0.5$, for different values of γ_{c_s}. There is an indication of counterion overscreening.
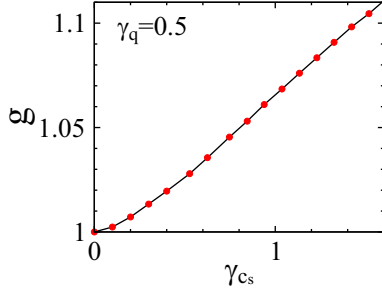
FIG. 16. Renormalization constant g as a function of γ_{c_s} for an electrolyte mixture of active coions and passive counterions.

"surface charge inversion." "Overscreening" can be traced to the divergent density profile, whose emergence is concurrent with dynamic adsorption. Even if a surface charge has not yet changed a sign, the released counterions that linger in the vicinity of a wall, together with adsorbed counterions, over-compensate a bare surface charge. "Overscreening," therefore, precedes and anticipates "surface charge inversion."

B. Passive counterions

As the last case study, we consider a mixture of active coions and passive counterions. In this case only coions become adsorbed, and the adsorbed coions renormalize a surface charge up. The renormalization constant for this situation is defined as $g = 1 + n_A^+/n$. Figure 16 shows g as a function of γ_{c_s}. As coions are generally depleted from a charged surface, the coion adsorption and the resulting charge renormalization are considerably weaker than that caused by active counterions.

VIII. CONCLUSION

In the present work we investigate a type of adsorption that arises in active dynamics and does not depend on the chemistry of a surface, as is the case with chemisorption and physisorption. The dynamic adsorption is particularly relevant for electrolytes, where the counterion adsorption renormalizes a surface charge down, and the coion adsorption renormalizes it up. The counterion adsorption, under some conditions, may lead to surface charge inversion. Then a divergent density near a charged wall, which is concurrent with dynamic adsorption, can lead to overscreening of a surface charge, prior to surface charge inversion. Far away from a wall, active dynamics modifies the screening of a surface charge, leading to a more diffuse double layer.

While these are all strictly dynamic effects, without direct counterpart in the passive system, there are some similarities with the behavior of Coulomb fluids in the vicinity of charge-disordered surfaces (diverging surface density of mobile charge [57]).

Based on the above conclusions one can state that the properties of active Coulomb fluids are unexpected and warrant further consideration, especially since addition of active charged particles to a colloid solution could pave the way to control and modify the electrostatics of colloids in the way that was impossible to contemplate from the mere passive particle perspective.

APPENDIX A: THE FOKKER-PLANCK EQUATION FOR ACTIVE PARTICLES

The probability distribution $\rho(\mathbf{r},\theta,\phi,t)$ of noninteractive active particles satisfy the following Fokker-Planck equation:

$$\frac{\partial \rho}{\partial t} = -\nabla \cdot \left\{ \left[v_0 \mathbf{n}(\theta,\phi) + \frac{\mathbf{F}(\mathbf{r})}{\zeta} \right] \rho \right\} + \frac{D_r}{\sin\theta} \frac{\partial}{\partial\theta} \left[\sin\theta \frac{\partial\rho}{\partial\theta} \right] + \frac{D_r}{\sin^2\theta} \frac{\partial^2\rho}{\partial\phi^2}, \quad \text{(A1)}$$

where $\mathbf{F}(\mathbf{r})$ is the external force. The above equation comprises two processes. The first process is simple convection, $-\nabla \cdot \mathbf{j}$, with the flux given by

$$\mathbf{j}(\mathbf{r},\theta,\phi,t) = \left[v_0 \mathbf{n}(\theta,\phi) + \frac{\mathbf{F}(\mathbf{r})}{\zeta} \right] \rho(\mathbf{r},\theta,\phi,t), \quad \text{(A2)}$$

where the flow is due to intrinsic particle force ζv_0 and an external force field $\mathbf{F}(\mathbf{r})$. The second process is the diffusion of a director vector $\mathbf{n}$ represented by an angular part of the Laplace operator with radius set to one. The combination of the two processes gives rise to active transport.

For a wall geometry considered in this work, where particles are confined to a half-space $z \geq 0$ and where an external force acts only in the z direction, $\mathbf{F} = (0,0,F)$, the relevant distribution is $\rho(z,\theta,t)$. Furthermore, as we focus on stationary distributions, the relevant differential equation is

$$\frac{\partial}{\partial z} \left\{ \left[v_0 \cos\theta + \frac{F(z)}{\zeta} \right] \rho(\theta,z) \right\} = \frac{D_r}{\sin\theta} \frac{\partial}{\partial\theta} \left[\sin\theta \frac{\partial\rho(\theta,z)}{\partial\theta} \right]. \quad \text{(A3)}$$

The application of the method of separation of variables assumes $\rho(z^*,\theta) = \Gamma(z^*)T(\theta)$. For noninteractive active particles in gravitational field the separation of variables yields two equations:

$$\frac{\partial \Gamma_n(z^*)}{\partial z^*} + 3\gamma_G \lambda_n \Gamma_n(z^*) = 0, \quad \text{(A4)}$$

$$\frac{\partial}{\partial\theta} \left[\sin\theta \frac{\partial K_n(\theta)}{\partial\theta} \right] + 6\gamma_G \lambda_n \sin\theta(\cos\theta - \alpha)K_n(\theta) = 0. \quad \text{(A5)}$$

APPENDIX B: THE MEAN-FIELD SIMULATION OF PASSIVE IONS: ANALYTICAL RESULTS

In this section we apply the mean-field simulation to passive counterions (or counterion sheets). For passive Brownian particles the weight of every configuration is proportional to the Boltzmann factor $e^{-U(z_1,...,z_n)/k_BT}$, where $U(z_1,\ldots,z_n)$ is the total electrostatic potential of the system. Analysis becomes more tractable if sheets are arranged into sequence [58,59],

$$0 \leq z_n \leq z_{n-1} \leq \cdots \leq z_2 \leq z_1 < \infty, \quad \text{(B1)}$$

so that the index i functions both as label and position index. A pair potential between any two sheets i and j is

$$\frac{u(z_i,z_j)}{k_B T} = \begin{cases} (z_i - z_j)/(n\lambda_{GC}), & \text{if } i < j \\ (z_j - z_i)/(n\lambda_{GC}), & \text{if } i > j, \end{cases} \quad \text{(B2)}$$

where λ_{GC} is the Gouy-Chapman length defined in Eq. (37). The factor $1/n$ indicates that the larger the number of sheets, the weaker the pair interactions. Taking into account the electrostatic potential due to a fixed charged wall at $z = 0$, $u_{\text{wall}}(z_i)/k_B T = z_i/\lambda_{GC}$, the total potential energy is found to be

$$\frac{U(z_1,\ldots,z_n)}{k_B T} = \frac{1}{n} \sum_{k=1}^{n} (2k-1)\frac{z_k}{\lambda_{GC}}, \quad \text{(B3)}$$

where the plate $k = 1$ feels the weakest potential, and the plate $k = n$ feels the strongest potential. The partition function can now be written as

$$Z_n = \prod_{k=1}^{n} \int_0^{z_{k-1}} dz_k\, e^{-(2k-1)z_k/(n\lambda_{GC})} = \frac{n^n \lambda_{GC}^n}{n!n!}, \quad \text{(B4)}$$

where $z_0 = \infty$. The limits of the integrals prevent positional permutations between sheets, which makes particles distinguishable, and there is no need of the factor $1/n!$.

Because sheets occupy different positions within a sequence, their distributions are unique, given by

$$p_m^{(n)}(z_m) = \frac{e^{-(2m-1)z_m/(n\lambda_{GC})}}{Z_n} \prod_{k=1}^{m-1} \int_{z_m}^{z_{k-1}} dz_k\, e^{-(2k-1)z_k/(n\lambda_{GC})}$$

$$\times \prod_{k=m+1}^{n} \int_0^{z_{k-1}} dz_k\, e^{-(2k-1)z_k/(n\lambda_{GC})}. \quad \text{(B5)}$$

The term of the first line evaluates to

$$\frac{Z_{m-1}}{Z_n} e^{-m^2 z_m/(n\lambda_{GC})} \quad \text{(B6)}$$

and is obtained by shifting all the variables of integration as $x_k = z_k - z_m$, which allows us to write

$$\prod_{k=1}^{m-1} \int_{z_m}^{z_{k-1}} dz_k\, e^{-(2k-1)z_k/(n\lambda_{GC})}$$

$$= \prod_{k=1}^{m-1} \int_0^{x_{k-1}} dx_k\, e^{-(2k-1)(x_k-z_m)/(n\lambda_{GC})}. \quad \text{(B7)}$$

The term of the second line is more difficult to evaluate but, after some manipulation, we get

$$2(-1)^m (n\lambda_{GC})^{n-m}$$

$$\times \sum_{k=m}^{n} \frac{(-1)^k k e^{-(k^2-m^2)z_m/(n\lambda_{GC})}(k+m-1)!}{(k-m)!(n+k)!(n-k)!}. \quad \text{(B8)}$$

A distribution for a plate m then becomes

$$p_m^{(n)}(z) = \frac{1}{n\lambda_{GC}} \frac{2(-1)^m n!n!}{(m-1)!(m-1)!}$$

$$\times \sum_{k=m}^{n} \frac{(-1)^k k e^{-k^2 z/(n\lambda_{GC})}(k+m-1)!}{(k-m)!(n+k)!(n-k)!}, \quad \text{(B9)}$$

where we drop the subscript m from z. From the identity

$$\sum_{k=m}^{n} \frac{(-1)^k (k+m-1)!}{k(k-m)!(n+k)!(n-k)!} = \frac{(-1)^m (m-1)!(m-1)!}{2\,n!n!}, \quad \text{(B10)}$$

we know that all the distributions $p_m(z)$ are normalized,

$$\int_0^{\infty} dz\, p_m^{(n)}(z) = 1. \quad \text{(B11)}$$

The charge distribution is obtained by summing up the distributions of all the sheets,

$$\rho_c^{(n)}(z) = \frac{\sigma_c}{n} \sum_{m=1}^{n} p_m(z), \quad \text{(B12)}$$

where the factor σ_c/n ensures that $\int_0^{\infty} dz\, \rho_c^{(n)}(z) = \sigma_c$, so that the charge density is independent of n. For the case $n = 1$, the distribution is exponential,

$$\rho_c^{(1)}(z) = \frac{\sigma_c}{\lambda_{GC}} e^{-z/\lambda_{GC}}, \quad \text{(B13)}$$

and corresponds to a one-particle distribution that is exactly the counterion density in the strong-coupling approximation [1]. Then, in the limit $n \to \infty$, we find

$$\rho_c^{(n)}(z) = \frac{\sigma_c/\lambda_{GC}}{(1 + z/\lambda_{GC})^2} + O\left(\frac{1}{n}\right), \quad \text{(B14)}$$

where the above expression is obtained by expanding the exponential term $e^{-k^2 z/(n\lambda_{GC})}$ in Eq. (B9). The dominant term corresponds to the solution of the Poisson-Boltzmann equation for the present problem; see Eq. (36).

In Fig. 17 we plot a number of charge density distributions for different values of n. Already for $n = 10$ the distribution is accurate up to the point $z/\lambda_{GC} \approx 10$, where the exponential decay takes over. For $n = 40$ the range of accuracy increases to $z/\lambda_{GC} \approx 100$. It appears then that the main size effect is the range of validity. For our simulations we use the values between $n = 1000$ and $n = 6000$, depending on the situation.
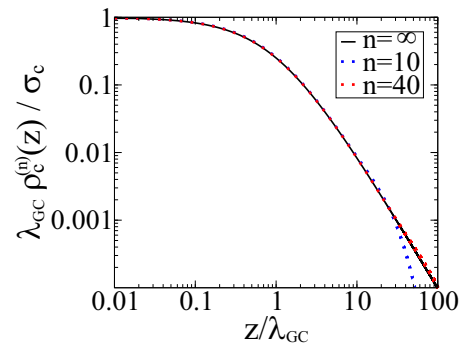

FIG. 17. Charge density distributions, $\rho_c^{(n)}(z)$, given in Eq. (B12), for different values of n.

[1] A. Naji, M. Kanduĉ, J. Forsman, and R. Podgornik, J. Chem. Phys. **139**, 150901 (2013).

[2] T. Markovich, D. Andelman, and R. Podgornik, in *Handbook of Lipid Membranes*, edited by C. Safynia and J. Raedler (Taylor & Francis, Philadelphia, in press).

[3] Y. Levin, Rep. Prog. Phys. **65**, 1577 (2002).

[4] D. Frydel and M. Ma, Phys. Rev. E **93**, 062112 (2016).

[5] Y. Xiang and D. Frydel, J. Chem. Phys. **146**, 194901 (2017).

[6] I. Borukhov, D. Andelman, and H. Orland, Phys. Rev. Lett. **79**, 435 (1997).

[7] D. Frydel and M. Oettel, Phys. Chem. Chem. Phys. **13**, 4109 (2011).

[8] D. Frydel and Y. Levin, J. Chem. Phys. **137**, 164703 (2012).

[9] D. Frydel and M. Oettel, in *Electrostatics of Soft and Disordered Matter*, Proceedings of the CECAM Workshop New Challenges in Electrostatics of Soft and Disordered Matter (Pan Stanford, Singapore, 2013).

[10] A. Abrashkin, D. Andelman, and H. Orland, Phys. Rev. Lett. **99**, 077801 (2007).

[11] M. Kanduč, A. Naji, Y. S. Jho, P. A. Pincus, and R. Podgornik, J. Phys.: Condens. Matter **21**, 424103 (2009).

[12] D. Frydel, J. Chem. Phys. **134**, 0234704 (2011).

[13] M. M. Hatlo, R. van Roij, and L. Lue, Europhys. Lett. **97**, 28010 (2012).

[14] D. Coslovich, J.-P. Hansen, and G. Kahl, Soft Matter **7**, 1690 (2011).

[15] D. Coslovich, J.-P. Hansen, and G. Kahl, J. Chem. Phys. **134**, 244514 (2011).

[16] D. Frydel and Y. Levin, J. Chem. Phys. **138**, 174901 (2013).

[17] P. B. Warren, A. Vlasov, L. Anton, and A. J. Masters, J. Chem. Phys. **138**, 204907 (2013).

[18] J.-M. Caillol and D. Levesque, J. Chem. Phys. **140**, 214505 (2014).

[19] D. Frydel, J. Chem. Phys. **145**, 184703 (2016).

[20] D. Frydel and Y. Levin, J. Chem. Phys. **148**, 024904 (2018).

[21] K. Bohinc, A. Iglič, and S. May, Europhys. Lett. **68**, 494 (2004).

[22] S. May, A. Iglic, J. Rescic, S. Maset, and K. Bohinc, J. Phys. Chem. B **112**, 1685 (2008).

[23] K. Bohinc, J. Rescic, J. Maset, and S. May, J. Chem. Phys. **134**, 07411 (2011).

[24] K. Bohinc, J. M. A. Grime, and L. Lue, Soft Matter **8**, 5679 (2012).

[25] D. Frydel, Adv. Chem. Phys. **160**, 209 (2016).

[26] C. F. Lee, New J. Phys. **15**, 055007 (2013).

[27] B. W. Ninham and V. A. Parsegian, J. Theor. Biol. **31**, 405 (1971).

[28] D. Chan, J. W. Perram, L. R. White, and T. W. Healy, J. Chem. Soc. Faraday Trans. I **71**, 1046 (1975).

[29] N. Adzic and R. Podgornik, Eur. Phys. J. E **37**, 49 (2014).

[30] N. Adzic and R. Podgornik, Phys. Rev. E **91**, 022715 (2015).

[31] T. Markovich, D. Andelman, and R. Podgornik, Europhys. Lett. **113**, 26004 (2016).

[32] T. Markovich, D. Andelman, and R. Podgornik, Europhys. Lett. **120**, 26001 (2018).

[33] L. Blum, M. L. Rosinberg, and J. P. Badiali, J. Chem. Phys. **90**, 1285 (1989).

[34] J. A. Greathouse and D. A. McQuarrie, J. Colloid Interface Sci. **175**, 219 (1995).

[35] J. A. Greathouse and D. A. McQuarrie, J. Colloid Interface Sci. **181**, 319 (1996).

[36] J. A. Greathouse and D. A. McQuarrie, J. Phys. Chem. **100**, 1847 (1996).

[37] N. J. Fisch and M. D. Kruskal, J. Math. Phys. **21**, 740 (1980).

[38] A. P. Solon, M. E. Cates, and J. Tailleur, Eur. Phys. J. Special Topics **224**, 1231 (2015).

[39] C. G. Wagner, M. F. Hagan, and A. Baskaran, J. Stat. Mech. (2017) 043203.

[40] C. Bechinger, R. Di Leonardo, H. Löwen, C. Reichhardt, G. Volpe, and G. Volpe, Rev. Mod. Phys. **88**, 045006 (2016).

[41] S. C. Takatori, R. Dier, J. Vermant, and J. F. Brady, Nat. Commun. **7**, 10694 (2016).

[42] J. Gao, P. Tang, Y. Yanga, and J. Z. Y. Chen, Soft Matter **10**, 4674 (2014).

[43] J. Z. Y. Chen, Prog. Pol. Sci. **54**, 3 (2016).

[44] E. P. Hsu, Summer School in Kyushu, 2008 (unpublished).

[45] M. Raible and A. Engel, Appl. Organometal. Chem. **18**, 536 (2004).

[46] R. G. Winkler, A. Wysocki, and G. Gompper, Soft Matter **11**, 6680 (2015).

[47] É. Mathieu, J. Math. Pure Appl. **13**, 137 (1868).

[48] L. Ruby, Am. J. Phys. **64**, 39 (1996).

[49] D. Frenkel and R. Portugal, J. Phys. A **34**, 3541 (2001).

[50] S. C. Takatori, W. Yan, and J. F. Brady, Phys. Rev. Lett. **113**, 028103 (2014).

[51] A. P. Solon, Y. Fily, A. Baskaran, M. E. Cates, Y. Kafri, M. Kardar, and J. Tailleur, Nat. Phys. **11**, 673 (2015).

[52] A. P. Solon, J. Stenhammar, R. Wittkowski, M. Kardar, Y. Kafri, M. E. Cates, and J. Tailleur, Phys. Rev. Lett. **114**, 198301 (2015).

[53] M. Krüger, A. Solon, V. Démery, C. M. Rohwer, and D. S. Dean, J. Chem. Phys. **148**, 084503 (2018).

[54] J. Dawson, Phys. Fluids **5**, 445 (1962).

[55] M. Antoni and S. Ruffo, Phys. Rev. E **52**, 2361 (1995).

[56] Y. Levin, R. Pakter, F. B. Rizzato, T. N. Teles, and F. P. C. Benetti, Phys. Rep. **535**, 1 (2014).

[57] M. Ghodrat, A. Naji, H. Komaie-Moghaddam, and R. Podgornik, J. Chem. Phys. **143**, 234701 (2015).

[58] A. Lenard, J. Math. Phys. **2**, 682 (1961).

[59] S. F. Edwards and A. Lenard, J. Math. Phys. **3**, 778 (1962).